frontiers in Materials

ORIGINAL RESEARCH
published: 03 February 2022
doi: 10.3389/fmats.2022.812738

Uniaxial Compression Damage Mechanical Properties and Mechanisms of Dolomite Under Deep High-Humidity Condition

Wei Chen[1], Wenqing Peng[2]*, Wen Wan[2]*, Xianqing Wang[2], Qiuhong Wu[2], Yu Zhou[2] and Senlin Xie[3]*

[1]Department of Building Engineering, Hunan Institute of Engineering, Xiangtan, China, [2]School of Resource, Environment and Safety Engineering, Hunan University of Science and Technology, Xiangtan, China, [3]School of Energy and Mining Engineering, China University of Mining and Technology (Beijing), Beijing, China

OPEN ACCESS

Edited by:
Erkan Oterkus,
University of Strathclyde,
United Kingdom

Reviewed by:
Xiaoping Zhou,
Chongqing University, China
Junhui Zhang,
Changsha University of Science and Technology, China

***Correspondence:**
Wei Chen
chenweiwade111@163.com
Wenqing Peng
pengwenqing111@163.com
Wen Wan
wanwenhunst@163.com

Specialty section:
This article was submitted to Mechanics of Materials, a section of the journal Frontiers in Materials

Received: 11 November 2021
Accepted: 05 January 2022
Published: 03 February 2022

Citation:
Chen W, Peng W, Wan W, Wang X, Wu Q, Zhou Y and Xie S (2022) Uniaxial Compression Damage Mechanical Properties and Mechanisms of Dolomite Under Deep High-Humidity Condition. Front. Mater. 9:812738. doi: 10.3389/fmats.2022.812738

The paper studies the uniaxial compression mechanical properties of pillars under the deep and high-humidity environment. We make the pillars cored from the −750 m mine room of Wengfu Phosphate Mine into the standard dolomite samples and test with a humidity control device developed by ourselves. Combining with uniaxial compression tests and microstructure inspections, we study the mechanical deterioration rule and damage mechanism of the dry samples and the wet ones that have been placed in a high-humidity condition (90% RH) for 30, 60 and 90 d, respectively. The results show that: 1) When the sample is placed in the humidity device, its original layered or sheet crystal morphology will change into sponge-like or flocculent morphology. As the placement time increases, the structure of the sample becomes looser and the boundaries between layers become blurred. The numbers of micro-cracks and micro-pores increase. 2) In the initial stage of water molecule intrusion (0–30 d), the strength and mass damages of the rock sample are less, and the damage rate is low. As high-humidity action time increases (30–90 d), the damage rates of both strength and mass gradually grow. 3) The failure modes of dolomites include shear failure and tensile/shear mixed failure, which are controlled by the storage time under high-humidity condition. As time goes by, more macroscopic cracks appear and the failure mode of the rock changes from shear to tensile. 4) Based on the X-ray diffraction and scanning electron microscopy analysis on mineral components, together with the principle of chemical kinetics, we discuss the chemical reaction process between dolomite and gaseous water molecules, and summarize the chemical damage mechanism of rocks during the water-rock interaction. The research has a certain guiding significance for the durability and stability prediction of pillars under deep high-humidity conditions.

Keywords: deep high humidity condition, water-rock interaction, ageing characteristics, damage mechanism, rock mechanics

1 INTRODUCTION

In the exploitation of non-metallic mines (especially some chemical mines), room and pillar mining is frequently applied to improve efficiency and save costs (Li et al., 2018; Cao S et al., 2020; Wang et al., 2020). The remaining pillars contain hydrophilic minerals (such as quartz, mica, etc.), which are easy to soften, hydrate, hydrolyze and dissolve in water (Lin et al., 2020; Liu et al., 2020; Zhang et al., 2020). As the shallow resources are gradually depleted, the mining industry develops in a deeper direction. The deeper mining makes ground temperature rise and groundwater develop. As a result, the evaporation increases and the relative humidity of the mine room reaches over 80% (He, 2014; Cao et al., 2021). Since the pillar in the deep room is eroded by water molecules for long time, its chemical dynamic process is closely related to the room stability, as well as the ground surface settlement (Hao et al., 2015; Chao, 2014). Besides, after a long-term geological tectonic process, numerous defects of different scales appear inside the pillars (Feng et al., 2021; Wang et al., 2019), and make the mechanical properties of the pillars more vulnerable to the high humidity (Yang and Liu, 2012; Zhou et al., 2019b).

As shown in **Figure 1**, the fractured pillars of the Baimuquan Phosphate Mine are eroded by gaseous water molecules due to the hydration under the high-humidity environment (Dunning et al., 1994; Cao et al., 2020a; Fan et al., 2021b). However, compared with the gaseous distilled water, the groundwater fluid contains various chemical components, which can cause not only the potential corrosion and dissolution of rock mass but also serious chemical corrosion to its physical structure (Fan et al., 2021a). The corrosions make the fractured pillars suffer both the overall deterioration and the microscopic structure destruction.

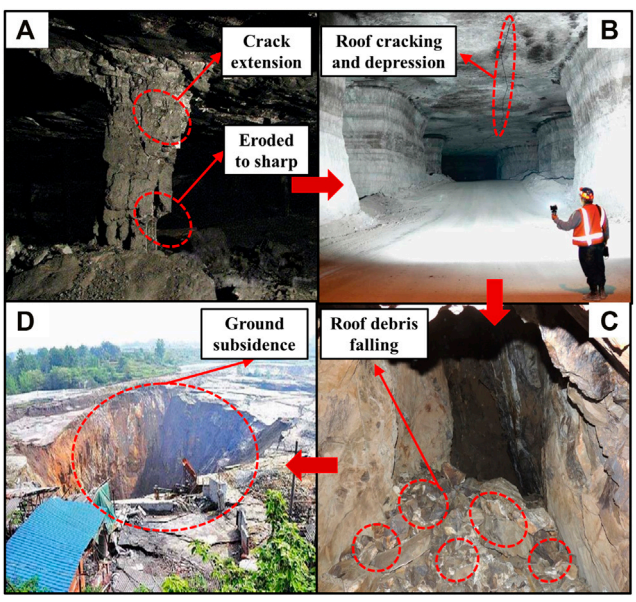

FIGURE 1 | Hydration and erosion of pillars under deep and high-humidity actions (Dunning et al., 1994): **(A)** Pillar instability; **(B)** Mine room Deformation; **(C)** Rockfall on the roof; **(D)** Land subsidence.

They accelerate the crack propagation and result in pillar instability, room damage, and surface settlement (Einstein et al., 1969; Esterhuizen et al., 2011; Li et al., 2018; Xie, 2019) (see **Figure 1**). Therefore, it is urgent to explore the damage mechanics characteristics of the pillars under the deep and high-humidity condition.

So far, scholars have carried out various experiments of water-rock interactions. They studied the chemical corrosion mechanism and establish related models. For instance, Zhao et al. (2018) investigated the deformation characteristics of the reservoir bank slopes under water-rock interaction. They found that the shear stiffness and strength degradations of joints, which are resulted from water-rock interaction, play a key role in the stability of reservoir bank slope. Miao et al. (2016) conducted uniaxial, triaxial, and Brazilian splitting tests on granite saturated in chemical solutions with different pH values and velocities. They compared the strength loss and deformation characteristics of granite. They also studied the influence of acid chemical corrosion on the microstructure, defect morphology, and mineral elements of granite with the scanning electron microscope and electron energy spectroscopy. Qiao's research shows that water has complex physical and chemical effects on rocks. The hydrophysical effects can lubricate and soften the interface between mineral particles and cement. They also erode, disperse, and transport mineral components. The hydrochemical effects are mainly the chemical reactions between unstable mineral particles and aqueous solutions (Qiao et al., 2017). Xie and Wan (2020) studied the acid-treated diorite and found that the mechanical properties of the acid-treated diorite decreased severely. Okubo et al. (2010) conducted uniaxial compression creep tests on tuff and andesite in dry and saturated states. Their results show that the creep strain of the saturated sample is greater than that of the dry one, while the creep failure strength of the saturated sample is less than that of the dry sample. Brzesowsky et al. (2014) studied how hydrochemistry and stress coupling can affect the creep of sandstone. Wang et al. (2019) carried out a triaxial creep test on shales immersed in solutions with different pH values, and established a creep constitutive model. They obtained the variation trend of shale creep parameters with solution acidity. Jiang and Wen (2011) made a uniaxial compression test on sandstones that have been eroded by acidic mine drainage (AMD) solution. They also established a damage constitutive model of sandstone under AMD erosion which can better reflect the evolution of sandstone damage. Moreover, Atkinson and Meredith (1981) and Dunning et al. (1994) found the influence of inorganic hydrochemical solutions on the fracture mechanical properties of quartz. Based on Griffith's strength theory, they made a theoretical analysis of the hydrochemical action mechanism on rocks.

According to the existing results on mechanical properties of water-rock interaction, most researches were carried out with rocks saturated in relevant solutions. However, the deep mine room provides high-humidity conditions (Liu et al., 2016; Chen et al., 2019), which means groundwater will hydrate with pillars in the form of gas. As for Wengfu Phosphate Mine in Guizhou Province, according to our hydrogeological investigation, weak

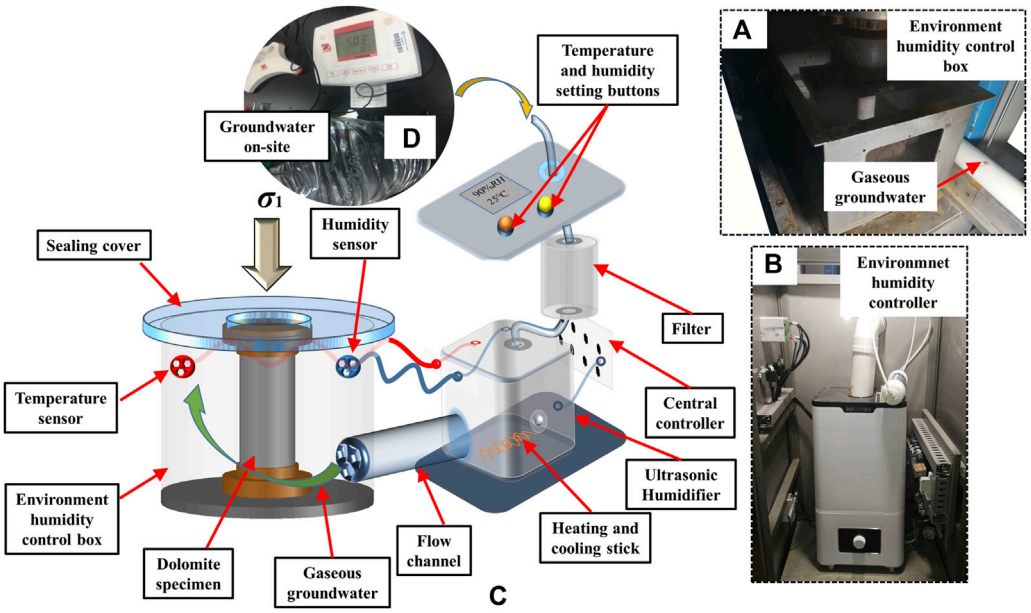

FIGURE 2 | Realisation of high-humidity environment: temperature and humidity environment control modeling device for rock mechanics experiments: **(A)** Environment humidity control box; **(B)** Environment humidity controller; **(C)** The diagram illustrating the operation of the device; **(D)** Groundwater taken on-site. (Chen et al.).

acidic groundwater exists in the −750 m mining section, and the pillars have been eroded by gaseous water for a long time. Therefore, in this paper, we prepare standard dolomite specimens by on-site coring, simulate a deep high-humidity environment, and do the uniaxial compression test with the MTS815 test system. Based on the test results, we analyze the time-dependent influence of the high humidity on the mechanical properties of specimens. We discuss the chemical reaction of specimens under the high humidity environment from the microscopic point of view (the X-ray diffraction and scanning electron microscopy observation). Finally, we summarise the mechanical damage mechanism.

2 LABORATORY TESTS

2.1 Realization of High-Humidity Conditions

The mechanical-humidity coupling of the pillar under the deep and high-humidity environment is the coupling formed under the condition that the specimen suffers the axis load and the gaseous groundwater invades into its micropores (Zhao et al., 2019a; Wu et al., 2020). To simulate the environment, we construct a device (see **Figure 2**) according to our patent "*Rock mechanics experiment temperature, humidity and acid environment control simulation device*" (patent no: ZL201920979019.3) (Chen et al.). The device consists of an enclosed box (see **Figure 2A**) and a controller (see **Figure 2B**). **Figure 2C** illustrates how it works. Firstly, the underground water taken from the site (see **Figure 2D**) is vibrated and vaporized by ultrasonic waves. Then it is transmitted to the box body through the pipeline. The humidity sensor and control unit in this box are used to keep the preset humidity.

2.2 Preparation of Rock Specimens

According to the environmental monitoring of line No.3–750 m middle section of the room-pillar mining area in Wengfu phosphate mine, the groundwater in this area develops and the relative humidity of the mine room is about 90% all year round (**Figure 3A–C**). As shown in **Figure 3D**, the mining area adopts the ordinary room-pillar method. We take part of pillar cores from the site, prepare them into standard cylindrical specimens of 50 × 100 mm (Cao et al., 2020b) (see **Figure 3E**) and seal them with plastic film to prevent weathering (Wu et al., 2019b; Zhao et al., 2019b). The saturated water absorption rate of the specimen is about 3.6% on average, measured with the boiling method. The average porosity of the specimen is 7.45%, tested with the AiniMR-60 nuclear magnetic resonance analyzer. Since the temperature of the mine area ranges from 25–30°C, floating within a minor scale (see **Figure 3A–C**), we set the testing temperature constantly at 25°C. The basic parameters of the tested dolomite are listed in **Table 1**.

2.3 Experiment Content and Test Method

The goal of our experiment on pillar specimens is to obtain the variation law of their mechanical properties and parameters under a high-humidity environment, as well as their failure deformation characteristics. Therefore, we carry out a variety of physical and mechanical tests in Work Safety Key Lab on Prevention and Control of Gas and Roof Disasters for Southern Coal Mine, Hunan University of Science and Technology, including electronic microscope scanning, X-ray diffraction

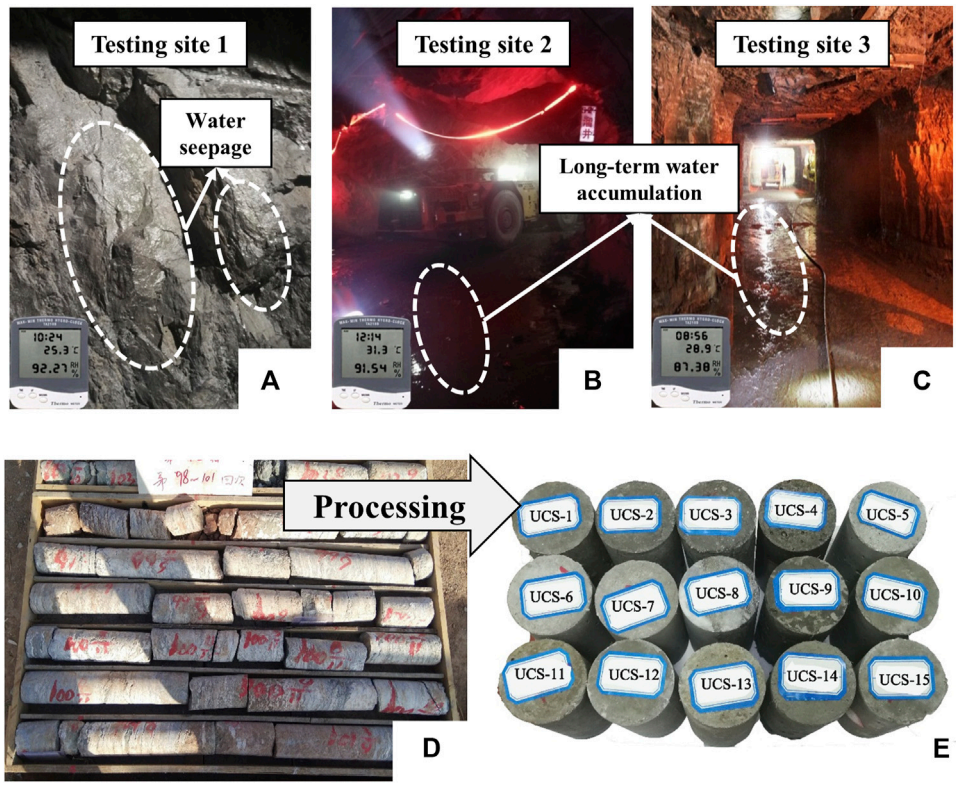

FIGURE 3 | On-site environment testing and sample production: **(A)** –750 m roadway surroundings; **(B)** –750 m opening bracket of ore pass; **(C)** –750 m mining chamber; **(D)** Taking cores; **(E)** Dolomite specimens.

TABLE 1 | The basic parameters of the dolomite samples.

Specimen number	Controlled humidity (% RH)	Average height (mm)	Average diameter (mm)	Average weight (g)	Average density (g/cm^3)	Placement time (d)
UCS-(1–5)	90	99.97	49.96	420.63	2.14	0
UCS-(6–10)		100.04	50.03	417.77	2.12	30
UCS-(11–15)>		99.95	49.93	422.57	2.15	60
UCS-(16–20)		100.03	50.01	418.07	2.13	90

and uniaxial compression test, before and after high-humidity treatment.

2.3.1 SEM Observation

In our SEM observation test, the samples are placed in a high-humidity environment with 90% RH for 90 days. The observations are performed every 30 days at 350 times magnification (see **Figure 4**).

2.3.2 X-Ray Diffraction Test

The X-ray diffraction (XRD) test is conducted as follows. Firstly, we grind the dolomite into powders of 10 μm, sprinkle the powders evenly on the sample holder and compact them with a glass plate, to make their surface flush with the glass (see **Figure 5B**). Then, we place the sample holder in the center of the goniometer and set the scanning parameters: the range is 50–650 μm, and the speed is 20 min. When the test completes, the analyzer automatically outputs the X-ray distribution curve, crystal plane spacing, count points and other data. According to the results of the XRD analysis (see **Figure 5C,D**), the main mineral components of dolomite are quartz, calcite and mica. Dolomite also contains a small amount of sodium feldspar, montmorillonite, illite and other minerals. The sample is dark green with a fine crystalline structure. Besides, it is relatively flat and presents a dense blocky structure.

2.3.3 Uniaxial Compression Test

The uniaxial compression test is performed with MTS-815 rock mechanics servo-controlled testing machine. Before the test, we store the dolomite specimens in the high-humidity environment

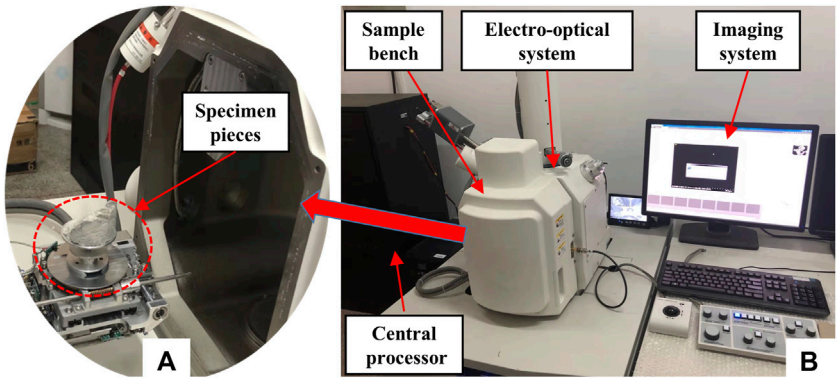

FIGURE 4 | SU3500 scanning electron microscope: **(A)** Stakeout table; **(B)** Operating platform.

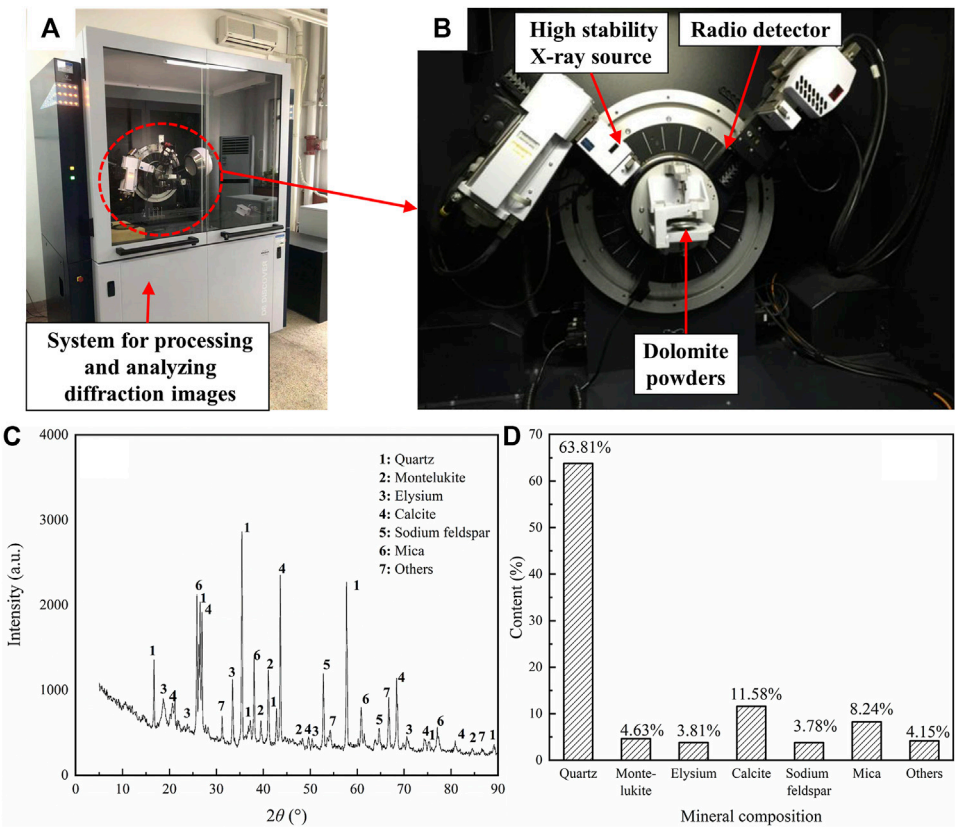

FIGURE 5 | XRD diffraction of ore pillar sample: **(A)** D8 advance XRD powder diffractometer; **(B)** Sample powder placement platform; **(C)** XRD spectrum of dolomite; **(D)** Determination result of mineral percentage content.

for 30, 60, and 90 d, respectively. During the test, the axial pressure is applied to the specimens with a rate of 0.2 kN/s. The loading rate is set at a relatively low level, to make the whole process of crack initiation, propagation, penetration and failure of the specimen be recorded with high-speed camera (Cao et al., 2019; Liu and Jiang, 2021). Meanwhile, we take the axial and cyclic displacement sensors to record the displacement of the specimen.

3 LABORATORY RESULTS AND ANALYSIS

3.1 Mass Damage Analysis

Due to the high-humidity action, the outer surface of dolomite is denuded and peeled off. The existence of natural fissures further causes chemical damages to the internal structure. Therefore, it is necessary to analyze the mass difference before and after the high-humidity action (Lin et al., 2020). To make accurate

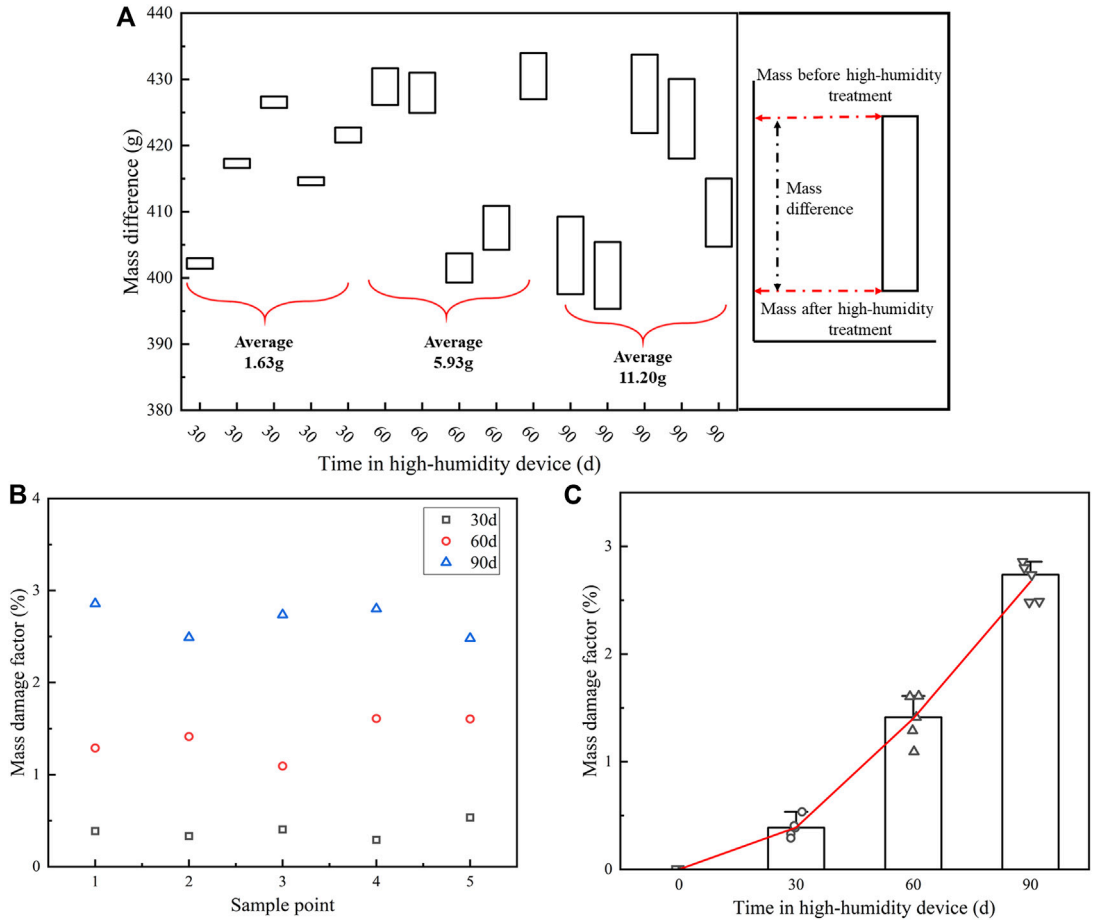

FIGURE 6 | Comparison of mass damage of dolomite at different time nodes under high-humidity action: **(A)** Mass damage of each sample; **(B)** Mass damage factor of each sample; **(C)** Mean and error of mass damage factors at each time node.

measurements, we wash the soaked specimens with distilled water, and dry them before weighing their messes with a precision balance. To quantitatively characterize the mass loss degree of the dolomite, a mass damage factor D is defined (see **Eq. 1**).

$$D_{(t)} = \frac{\Delta M_{(t)}}{M_0} \times 100\% = \frac{M_0 - M_{(t)}}{M_0} \times 100\% \quad (1)$$

In **Eq. 1**, M_0 is the initial mass of the specimen, $M_{(t)}$ is its mass after t days under the high-humidity condition, and $\Delta M_{(t)}$ is the mass difference before and after treatment in high-humidity environment for t d. We take five specimens as a group and store them under high-humidity environment for the same period. **Figure 6** shows the mass differences and the mass damage factors of specimens at different time nodes.

According to **Figure 6A**, the mass of the rock sample decreases to a varying degree under the high-humidity condition, while the decrease rate gradually increases with the action time. To be specific, the average mass loss of specimen is 11.20 g after 90 d's high-humidity action, which is 1.89 and 6.87 times higher than that after 60 and 30 d, respectively. Meanwhile, the mass damage factor of specimens under high-humidity action for 90 d is significantly greater than those for 60 and 30 d. The mean value is 2.73%, which is 1.94 and 7.18 times higher than that for 60 and 30 d, respectively (see **Figure 6B,C**). Besides, as the high-humidity action time increases, acidic molecules in the air permeate the sample deeper, and lead to the fracture of chemical bonds between mineral grains. Besides, the internal expansion of the sample intensifies the fall of powders and debris from the surface. It means that the longer high-humidity action time can result in more serious physical structure damage (Zhao et al., 2017).

3.2 Deterioration of Dolomite Mechanical Properties Under High-Humidity Condition

3.2.1 Degradation Law of the Uniaxial Compressive Strength of Dolomite

According to 20 groups of test results, the basic mechanic parameters such as peak strength, elastic modulus and Poisson's ratio of dolomite under uniaxial compression tests are obtained at different high-humidity treatment times and summarized in **Table 2**.

TABLE 2 | Uniaxial compression mechanic parameters of dolomite at each high-humidity action time node.

Specimen number	Controlled humidity (% RH)	Placement time (d)	Peak strength (MPa)	Modulus of elasticity (GPa)	Poisson's ratio
UCS-1	90	0	26.39	5.43	0.15332
UCS-2		0	26.45	5.36	0.15541
UCS-3		0	26.67	5.46	0.15326
UCS-4		0	25.95	5.34	0.15763
UCS-5		0	25.70	5.41	0.16348
UCS-6		30	25.25	4.93	0.15642
UCS-7		30	25.38	4.86	0.15952
UCS-8		30	24.94	4.91	0.15945
UCS-9		30	24.79	4.92	0.15983
UCS-10		30	24.60	4.73	0.15883
UCS-11		60	22.14	3.76	0.16168
UCS-12		60	21.99	3.73	0.16498
UCS-13		60	21.96	3.74	0.16126
UCS-14		60	21.68	3.77	0.16265
UCS-15		60	21.58	3.76	0.16108
UCS-16		90	19.21	3.13	0.17446
UCS-17		90	19.27	3.08	0.17387
UCS-18		90	19.12	3.13	0.16954
UCS-19		90	18.87	3.12	0.16576
UCS-20		90	18.93	3.13	0.17442

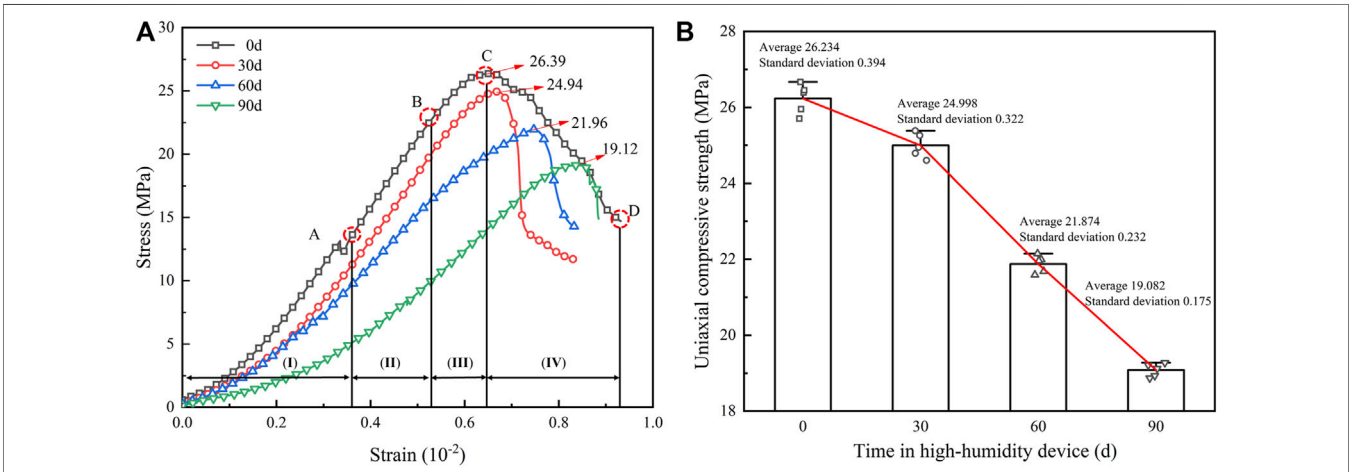

FIGURE 7 | Uniaxial compression law of dolomite samples under different high-humidity times: **(A)** Stress-strain curves; **(B)** Uniaxial compressive strength.

For each placement time, the dolomite with the median peak uniaxial compressive strength is selected as the representative to draw the stress-strain curve. As shown in **Figure 7A**, all specimens under load have experienced four typical stages until failure: initial crack compaction stage (I), elastic deformation to micro elastic fracture stable development stage (II), unsteady fracture development stage (III), and post-peak stage (IV) (Zhao et al., 2017; Wang and Wan, 2019). They have different characteristics due to different high-humidity action times. (I) In the initial stage of fracture compaction, the concave degree on the curve decreases with high-humidity action time. It indicates that the defects in the dolomite increase due to long-term hydration, so the number of newly generated micro-cracks under uniaxial compression decreases (Zhao et al., 2019a; Zhao et al., 2021b). (II) In the elastic deformation to micro elastic fracture stable development stage, the slope of the curve gradually decreases with longer high-humidity action time. It shows that the elastic modulus also gradually decreases. (III) In the unsteady fracture development stage, stress-strain curves of the samples after the high-humidity treatment quickly drop after the peak strength, showing typical brittle failure feature. Meanwhile, the peak stress of the rock sample decreases significantly from 26.39 MPa (dry) to 19.12 MPa (90 d), which declined by 27.26%. However, the peak strain of the sample increases from 0.65×10^{-2} (dry) to 0.84×10^{-2} (90 d) with longer high-humidity action time, which increases by 29.21%. A small stress platform appears nearby the peak value, which is caused by the gradual deformation and failure around the crack (Liu et al., 2018). (IV) In the post-peak stage, the dried specimens are low brittle and high plasticity, which still provides greater deformation,

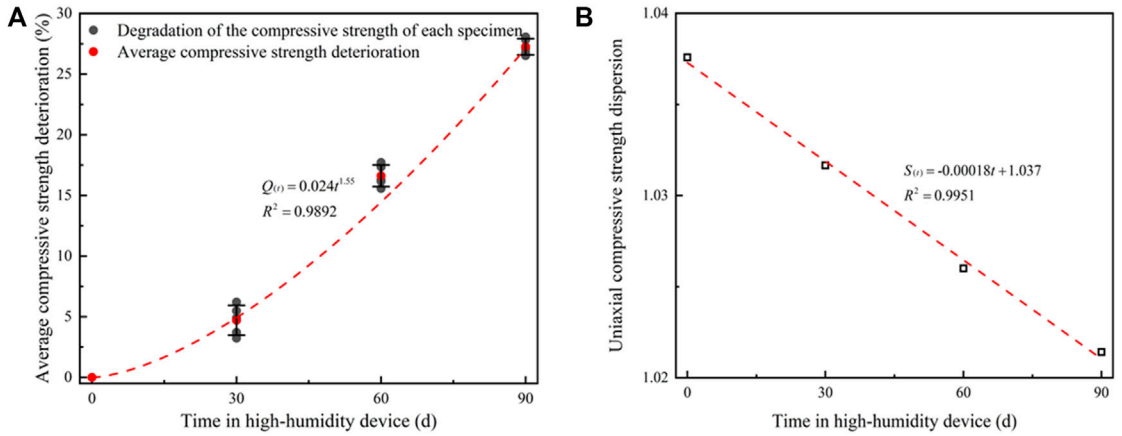

FIGURE 8 | Uniaxial compressive strength law: **(A)** the degradation of dolomite uniaxial compressive strength under different high-humidity action times; **(B)** trends in uniaxial compressive strength dispersion of dolomite under different high-humidity action times.

indicating that the dried specimens are dense (Zhao et al., 2021a). On the contrary, the internal structure of the samples treated with high-humidity is loose due to hydration, and the brittleness increases due to the lack of cement between particles. Finally, through quantitatively analyzing the degradation law of the mechanical properties of rock samples under different high-humidity times, the compressive strength of the rock samples is calculated and plotted as shown in **Figure 7B**.

Figure 7B shows that the uniaxial compressive strength of dolomite decreases gradually with high-humidity action time. The corresponding curve of compressive strength versus time gradually moves down, which is consistent with the previous similar test results (Miao et al., 2016).

To better analyze the impact of different high-humidity action times on the mechanical properties of rock samples, the degree of deterioration $Q_{(t)}$ is defined as follows (Deng et al.; Wu et al., 2019a):

$$Q_{(t)} = \frac{\sigma_0 - \sigma_{(t)}}{\sigma_0} \times 100\% \tag{2}$$

In **Eq. 2**, $\sigma_{(t)}$ represents the uniaxial compressive strength of the rock sample placed under high-humidity environment for t d. s_0 is the uniaxial compressive strength of the rock sample under natural dry state condition. The typical stage deterioration of dolomite is shown in **Figure 8**.

Figure 8A shows that the compressive strength of the rock sample decreases gradually with high-humidity action time, but the degradation range is non-uniform. The degree of degradation caused by high-humidity is small from 0 to 30 d, while it increases significantly afterward. The distribution curve conforms to the power function growth, with a high agreement degree (Zhang et al., 2021). Compared with the dry rock samples, the degradation degree of the samples after 30, 60, and 90 d's high-humidity treatments is 4.71%, 16.62% and 27.26% respectively. Besides, the deterioration law shows that the difference of uniaxial compressive strength deterioration of the specimens decreases gradually with the high-humidity action time. According to the evaluation method of rock mass dispersion under different humidity action times (Deng et al.), we take the ratio of maximum and minimum compressive strength of rock sample as its dispersion degree, and express as S. The specific statistical results are shown in **Figure 8B**. As high-humidity time increases, the uniaxial compressive strength dispersion of the dolomite decreases and presents a linear distribution. The degree of dispersion decreases from 1.04 (dry) to 1.02 (90 d), indicating that high-humidity action time has a certain inhibitory effect on the dispersion.

3.2.2 Mechanical Parameter Degradation Law of Dolomite

The elastic modulus E and Poisson's ratio μ are two important parameters that express the mechanical deformation characteristics, which are generally calculated with the average modulus of elasticity (**Eq. 3**) and Poisson's ratio (**Eq. 4**). The result is shown in **Figure 9**.

$$E = \frac{(\sigma_B - \sigma_A)}{(\varepsilon_{hB} - \varepsilon_{hA})} \tag{3}$$

$$\mu = \frac{(\varepsilon_{dB} - \varepsilon_{dA})}{(\varepsilon_{hB} - \varepsilon_{hA})} \tag{4}$$

In **Eq. 3** and **Eq. 4**, σ_A and σ_B are the stress of the start point A and the end point B of the approximate linear part of the stress-strain curve. ε_{hA}, ε_{dA}, ε_{hB} and ε_{dB} are the axial and radial strains corresponding to points A and B (see **Figure 7A**).

The modulus of elasticity is less affected by the test conditions (its main influence factor is the loading method), so it can accurately reflect the effect of high-humidity on the axial deformation characteristics. The Poisson's ratio is greatly affected by the test conditions, including the testing machine, the deformation measurement method, the loading control method, and the loading rate (Gercek, 2007). Therefore, to

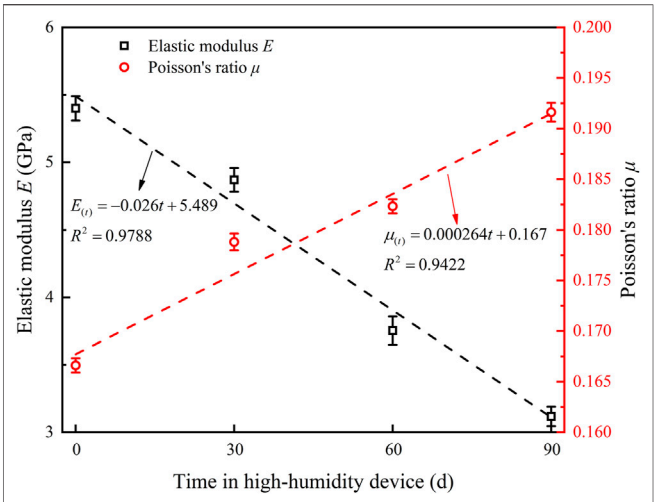

FIGURE 9 | Effect of high-humidity action time on the modulus of elasticity and Poisson's ratio of dolomite.

accurately reflect the damage of high-humidity on dolomite, the consistency of test conditions should be ensured.

Figure 7A and **Figure 9** show that the deformation of the dolomite specimen in the approximate straight section generally decreases after the high-humidity treatment, which means the elastic modulus reduces. The elastic modulus is linearly related to high-humidity action time, the R^2 value is close to 1, indicating positive fitting (Zhang J.-Z et al., 2019). After 90 days under high-humidity (90% RH), the elastic modulus of dolomite decreased by 42.26% compared with the dry state. Although the heterogeneity of the rock and the difference of chemical corrosion lead to the discreteness of the strength and deformation, it is still obvious that the elastic modulus of dolomite is very sensitive to environmental humidity.

As shown in **Figure 9**, Poisson's ratio of dolomite is also sensitive to the high-humidity environment. After high-humidity treatment, the Poisson's ratio of the specimen grows linearly to varying degrees. For instance, after being placed in the high-humidity environment for 90 d, the Poisson's ratio of the dolomite increases by 14.99% compared to the dry state.

3.3 Analysis of Dolomite Failure Modes Under High-Humidity Condition

The ultimate failure mode is one of the most popular topics in rock mechanics research (Zhao et al., 2016; Zhang J.-Z. etal., 2019; Zhang and Zhou, 2020a). When the rock specimen is damaged under uniaxial compression, it is only subjected to axial stress, with no lateral pressure (Zhou et al., 2019a). Therefore, the failure and deformation of the specimen are generally not limited (Zhou et al., 2018). The specific failure modes of the rock specimen under uniaxial compression are shown in **Figure 10**. Rock under uniaxial compression can usually produce three types of failure modes, including X-shaped conjugate inclined plane shear failure (see **Figure 10A**), single inclined plane shear failure (see **Figure 10B**), and tensile failure (see **Figure 10C**). Among them, X-shaped conjugate inclined plane shear failure is the most common one, as well as single inclined plane shear failure, are caused by the shear stress on the failure surface exceeding the strength limit of the rock sample, so they both belong to shear failure (Zhou and Zhang, 2021). Since the shear stress that the failure surface needs to withstand before failure is related to the normal stress, this type of failure is also called compression-shear failure (Zhang J.-Z. et al., 2019). Moreover, the tensile failure is caused by the Poisson effect. Under the action of axial stress, the transverse tensile stress generates. When the transverse tensile stress exceeds the tensile limit of the rock, tensile failure occurs (Wang et al., 2021).

According to the test results, the ultimate failure modes of rock samples under different high-humidity time nodes mainly include shear failure and shear/tension mixed failure. As shown in **Figure 11**, the rock sample in the dry state mainly exhibits shear failure, and the failure mode changes to tensile failure as high-humidity action time increases. For example, on day 60 and day 90, the mixed shear/tensile failure mode becomes the main choice of rock samples. Before being loaded, the internal defects of the dried sample have formed a stable mechanical state under the long-term ground stress. So there are fewer cracks on the sample surface when it is loaded. However, the internal structure of the sample has changed after the high-humidity treatment. Therefore, under the same loading rate, the development of cracks and particles is rearranged. The internal defects and surface cracks of the sample are fully developed again, which manifest as the newly generated macrocracks.

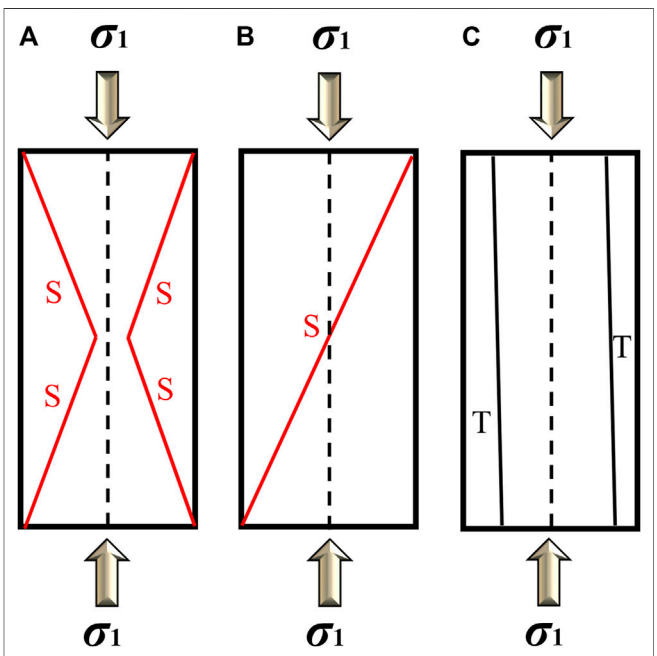

FIGURE 10 | Uniaxial compression test force and failure modes of specimens: **(A)** X-shaped conjugate inclined plane shear failure mode; **(B)** Single inclined plane shear failure mode; **(C)** Tensile failure mode (Zhang and Zhou., 2020b; Zhao et al., 2021b).

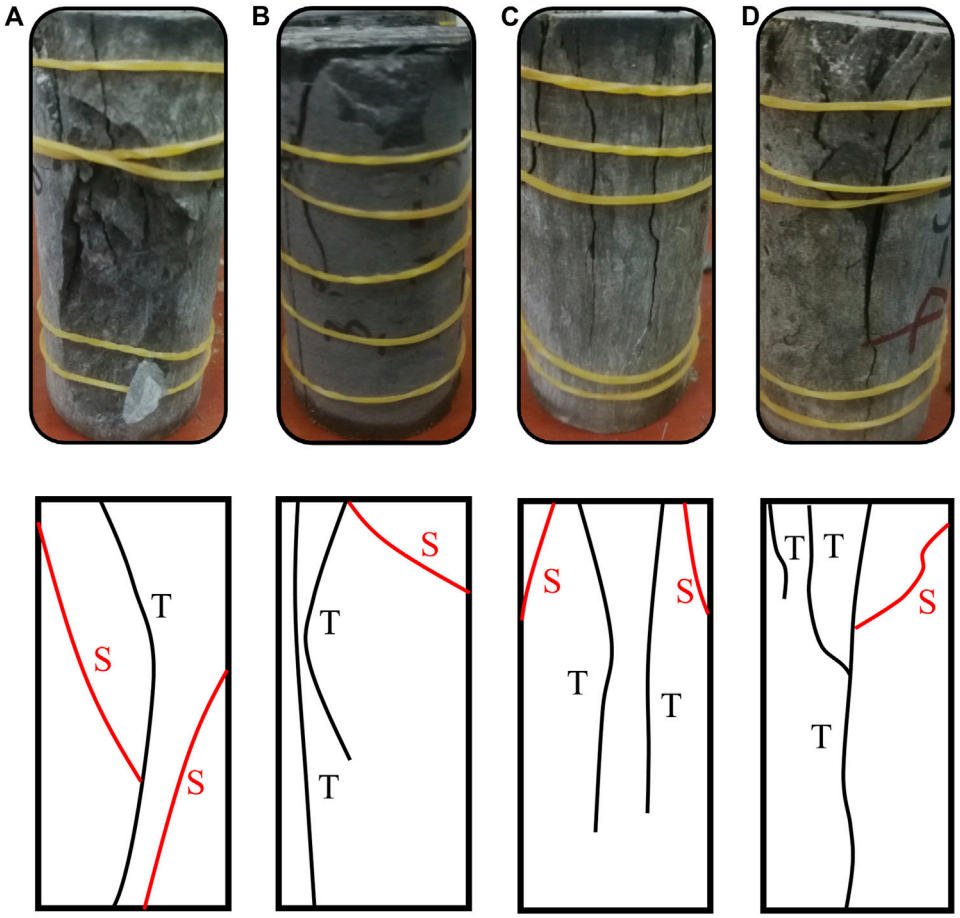

FIGURE 11 | Failure modes of rock samples under different high-humidity action time: **(A)** 0 d; **(B)** 30 d; **(C)** 60 d; **(D)** 90 d.

4 DISCUSSION ON DAMAGE MECHANISM OF HIGH-HUMIDITY

4.1 Microscopic Damage of Dolomite Under High-Humidity Condition

Figure 12A shows that the surface of the dried specimen presents a clear lamellar structure or lamellar crystalline morphology, which has good homogeneity and a relatively tight internal structure with small interlayer distances. The microcracks and micropores are small in size and dispersed, while few large-sized pores exist. The particles in this microstructure are homogeneous and compact, with fine and sparse pores. They reflect good macro-mechanical properties of dolomite before high-humidity action.

After 30 days of high-humidity action, the original layered structure or flaky crystal form of rock shows a sponge-like or flocculent morphology. Moreover, the degree of structural looseness increases, the boundary between the layers becomes blurred, and the cement between the grains disappears with hydration. Thus, the "gullies" of varying sizes are formed (see **Figure 12B**). When high-humidity action time reached 60 d, the particles on the outer surface loosen and fall with hydration. The internal "gully" gradually develops into micro-cracks. The surface structure becomes loose, accompanied by the development of secondary pores. The dissolution effect is obvious (see **Figure 12C**). On the 90th day, many small pores appear on the crystal surface of the sample. These small pores are in honeycomb structures. And there is no cementation between the minerals. The large crystal particles transform into lots of small clastic particles. The regular-shaped crystal particles no longer exist, and the micro-structure damage of the rock sample becomes more and more serious (see **Figure 12D**). It macroscopically presents as the deterioration of the sample mass, which also shows the microscopic mechanism of the high-humidity environment damages on the physical and mechanical parameters of the pillar.

4.2 Changes in Mineral Composition of Dolomite Under High-Humidity Action

Through the X-ray diffraction analysis on the sample powders at various time nodes under high-humidity action (see **Figure 13A–D**), we get the mineral composition comparison in **Figure 13E** by JADE software. It shows that the contents of quartz (SiO_2), calcite ($CaCO_3$), albite ($NaAlSi_3O_8$) and mica [$KAl_3Si_3O_{10}(OH)_2$] decrease to varying degrees with high-

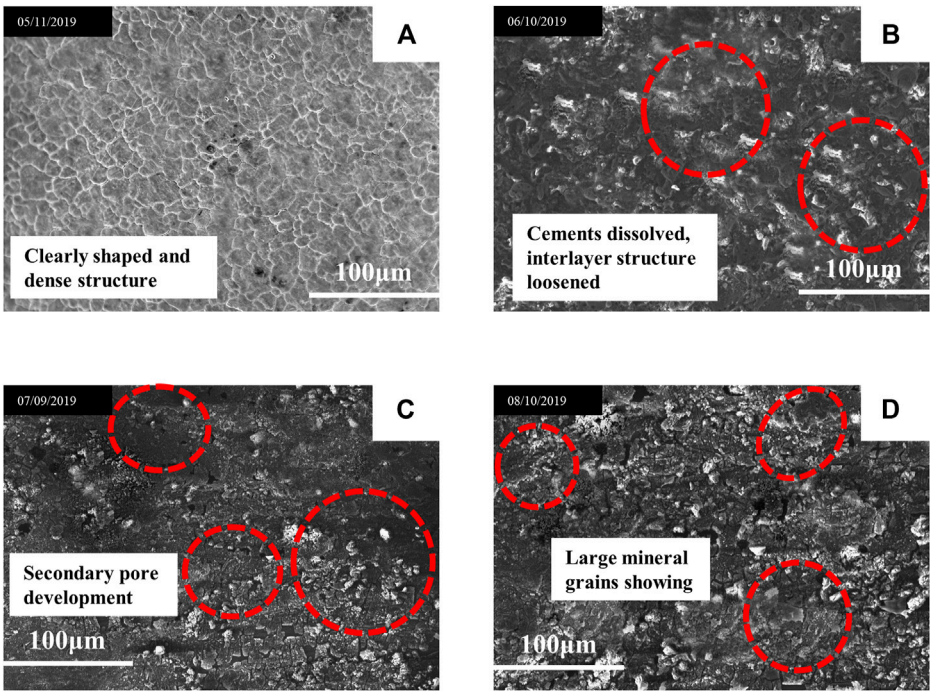

FIGURE 12 | Scanning electron microscope images of dolomite under different high-humidity action times: **(A)** 0 d; **(B)** 30 d; **(C)** 60 d; **(D)** 90 d.

humidity action time, while the content of kaolinite [$Al_2Si_2O5(OH)_4$] has a certain increase. Based on the chemical dynamic reaction process (Zhao et al., 2017) and the analysis of scanning electron microscope images, the reaction between dolomite and acid gaseous water is summarized as follows:

4.2.1 Corrosion

At the microscopic contact interface between the acid gaseous water molecules and the sample, the soluble minerals encounter H^+ and quickly dissolve to release Ca^+, Mg^{2+}, and Na^+ (Miao et al., 2016; Chen et al., 2019). These active cations dissolve the main minerals of the rock mass continuously, which loosen the structure between the rock particles. They also accelerate the entry of water molecules into the open pores or dissolution pores between the rock particles.

$$CaCO_{3(s)}+2H^+_{(aq)} \rightarrow Ca^{2+}_{(aq)}+CO_{2\,(aq)} + H_2O_{(l)} \quad (5)$$

(Dissolution of calcite, release of Ca^{2+}).

Besides, detrital minerals transform into clay minerals due to the acid gaseous water dissolution. Through the X-ray diffraction analysis, it can be seen that the main detrital minerals in the dolomite pillars are albite and mica. The edges of detrital minerals eroded by acidic water molecules are blurred. Dissolution holes appear. And the detrital minerals are eroded into kaolinite. The chemical reaction that occurred is:

$$2NaAlSi_3O_{8(s)}+2H^+_{(aq)}+9H_2O_{(g)} \rightarrow Al_2Si_2O_5(OH)_{4(s)} + 2Na^+_{(aq)}+4H_4SiO_{4(l)} \quad (6)$$

(Dissolution of albite, release of Na^+ and formation of kaolinite)

$$KAl_3Si_3O_{10}(OH)_{2(s)} + H^+_{(aq)}+1.5H_2O_{(g)} \rightarrow 1.5Al_2Si_2O_5(OH)_{4(s)} + K^+_{(aq)} \quad (7)$$

(Dissolution of mica, release of K^+ and formation of kaolinite).

4.2.2 Hydration

After contacting with the gaseous hydrochloric acid solution, K^+, Na^+, Mg^{2+} and other cations in dolomite mineral components exchange with hydroxyl ions. It leads to mineral hydration, which further forms relatively stable mineral compositions. However, due to the effect of ion exchange, the volume of the newly formed mineral reduces. It also forces the porosity of the surface layer of the pillar to decrease and the cementation between grains to weaken. Taking quartz and albite as an example, their hydration happens as follows:

$$SiO_{2(s)}+2H_2O_{(g)} \rightarrow H_4SiO_{4(l)} \quad (8)$$

(Quartz hydration produces protosilicate).

The dissolution degree of calcite, dolomite and other carbonate minerals increase significantly at 25°C, atmospheric pressure and acid solution. The dissolution reaction equation is:

$$4NaAlSi_3O_{8(s)}+6H_2O_{(g)} \rightarrow Al_4Si_4O_{10}(OH)_{8(s)}+8SiO_{2(s)} + 4NaOH_{(l)} \quad (9)$$

(Albite hydration produces kaolinite and silica colloid).

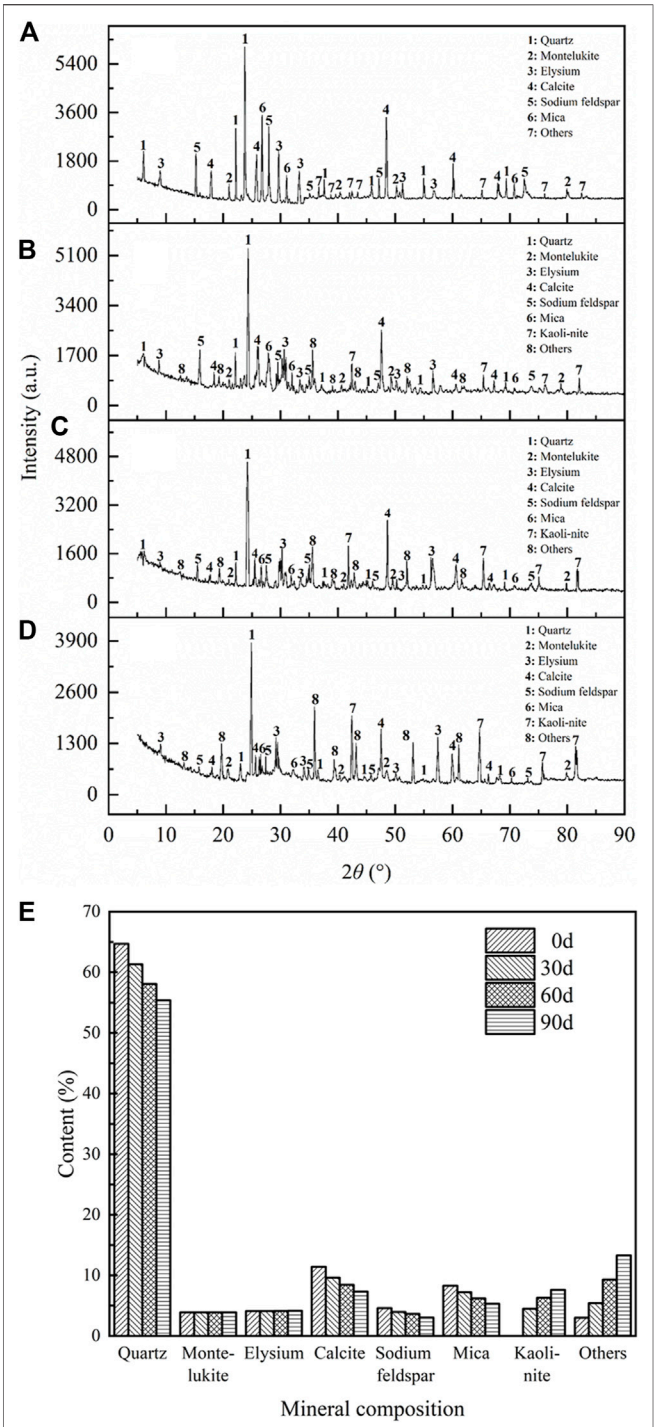

FIGURE 13 | X-diffraction patterns of sandstone specimens at various time nodes under high-humidity action: **(A)** 0 d; **(B)** 30 d; **(C)** 60 d; **(D)** 90 d; **(E)** the percentage of the main mineral content of the specimen at different time nodes of high-humidity.

4.2.3 Water Swelling and Disintegration of Clay Minerals

Both mechanisms 1) and 2) make the dolomite generate lots of kaolinite (**Figure 13**), which is mainly composed of $Al_2Si_2O_5(OH)_4$. Together with the montmorillonite contained in the dolomite itself, there exist two typical clay minerals. When clay mineral undergoes a high-humidity process, it has high hydrophilicity and obvious hydration expansion characteristics. These characteristics can result in cementation decrement between mineral particles and rapid volume increment of clay minerals, which eventually cause damage inside the rock. Moreover, the clay mineral particles are very small (≤2 μm) and have larger surface energy. Their interlayers can be easily occupied by water molecules and form layers of polarized water molecules. The polarized water molecular layer continuously absorbs water and expands the interlayer expansion, which makes the water molecules enter into the middle layer of mineral crystal cells and form a water layer interlayer inside the minerals. It results in the expansion of clay minerals and increases the volume of rock mineral crystals. Since the swelling force generated by the water absorption of clay minerals is not uniform, the cell spacing will increase and the cement connecting between mineral particles will be damaged. As time goes by, the mineral structure of the pillar eventually decomposes under the high-humidity condition. The components lose contact, and the interior gradually disintegrates. The chemical formulas of water swelling of clay minerals (kaolinite, montmorillonite) are as follows:

$$Al_4Si_4O_{10}(OH)_{8(s)}+nH_2O_{(g)} \rightarrow Al_4Si_4O_{10}(OH)_{8(s)}\bullet nH_2O_{(s)} \tag{10}$$

(Water swelling of kaolinite)

$$Si_6A_4MgFe_3Na_4O_{20}(OH)_{4(s)}+nH_2O_{(g)} \rightarrow Si_6A_4MgFe_3Na_4O_{20}(OH)_4\bullet nH_2O_{(s)} \tag{11}$$

(Water swelling of montmorillonite).

4.3 Mechanical Damage Mechanism of Dolomite Under High-Humidity Condition

High-humidity has a significant effect on the mechanical parameters' deterioration of dolomite. Compared with the dry state, the peak strength and elastic modulus of the samples after 90 days of high-humidity treatment decreased by 27.26 and 42.26%, respectively. But the peak strain and Poisson's ratio rise by 29.21 and 14.99%. The influence mechanism of high-humidity on the mechanical parameters of dolomite is described as follows.

As a typical sedimentary rock, dolomite has initial defects that make it easy to be permeated by gaseous water molecules. Under a high-humidity environment, the surface and primary microcracks of the specimen can contact more water molecules. Some minerals in the specimen suffer ion exchange and hydrolysis and form secondary minerals kaolinite and silica. Kaolinite, silica and some original component of rock, such as illite and montmorillonite are all hydrophilic minerals. They have strong water absorption and expansion characteristics, which can result in differences between the internal and external stress and leads to the falling of mineral particles from the outer layer of the

rock. As a result, the micropores and fissures gradually develop. During the water-absorbing process, the infiltration of water molecules makes the framework of mineral particles lubricated and softened, thus promoting the water-rock interaction in calcareous cement and feldspar minerals. The stress concentration at the pore and crack tip of the rock further promotes the propagation of microcracks. During the drying process, water molecules evaporate. Some water-soluble minerals generated by water-rock interaction migrate outward with water molecules, which promotes the formation of micropores and permeability channels. Moreover, some secondary minerals crystallize and expand, leading to the development of pores and fissures among mineral particles. New water-rock interaction reaction surfaces are formed.

Based on the above changes, the mineral grain framework of dolomite becomes soft. The internal microscopic pores and cracks develop. Furthermore, the overall structure of the rock sample tends to loosen and soften. These changes eventually lead to the evolution of the microscopic structure. Meanwhile, the change of microstructure of rock reduces the compactness of the sample, which leads to the deterioration under high-humidity. The deterioration of the dolomite specimen gets more severe with longer high humidity action, which presents as the decrement of peak strength and elastic modulus, as well as the increment of the peak strain and Poisson's ratio. It is also the fundamental reason for the deterioration of mechanical properties and the change of failure mode. As the research object of this paper refers dolomite pillar, the effect of the confining pressure was not considered in the mechanical tests. Therefore, regarding the roadway surrounding rock under three-way stress, we will proceed with further analysis of high-humidity impacts on the triaxial compression mechanical parameters of the surrounding rock specimens.

5 CONCLUSION

In light of the above work, the main conclusions of this paper are as follows:

1) As the high-humidity action time increases, the original dense flake crystal morphology of dolomite presents a flocculent morphology. Its structure becomes more looseness. Meanwhile, the boundary between layers becomes blurred, the number of micro-cracks and micro-pores increases. Furthermore, the mineral particles soften and decompose, which makes the microstructure of dolomite develop from a relatively dense state to porous. The overall structure of dolomite tends to loosen and the mass decreases.
2) The high-humidity action deteriorates the mechanical parameters of the specimen. As the action time increases, the elastic modulus and peak strength of the specimen decrease, while the Poisson's ratio and peak strain increase. With a longer high-humidity action time, the anisotropy of the dolomite will be restrained. The specimen absorbs water molecules from the air and generates water pressure. The pressure splits the original cracks in the specimen and weakens the friction between the crack surface and particles. As a result, the crack propagation and the dolomite failure are accelerated. The failure mode changes from shear to shear/tension mixed failure.
3) The key factor for room and pillar mining is the mechanical stability of the pillar. As the object of this research are pillars, they are generally under compression at the top and bottom ends. Therefore, we only consider the uniaxial compression mechanical properties of the specimens and have not regarded the effect of the confining pressure in this experiment. Through our research, three chemical damages have been found on the water-rock contact interfaces of the dolomite pillars under the high-humidity condition (90% RH), due to the existence of hydrophilic minerals. As the excavation of the -750 m level mine rooms is completed, the Wengfu Phosphorus mineshaft project will be developed further downwards. The humidity condition will be more severe. Moreover, due to the long-term deep high ground stress, the acquired fissures in pillars will be more complicated in shape, amount and size. If such pillars continue to be used, their mechanical properties must be weaker than those under the humidity condition of 90% RH. Meanwhile, regarding chemical mines in other regions operating at depth, it is necessary to make proper underground ventilation and dehumidification of the mine room to reduce the later workloads and the duration of the rehabilitation work. It can significantly save pillar protection costs and improve mining efficiency.

DATA AVAILABILITY STATEMENT

The raw data supporting the conclusion of this article will be made available by the authors, without undue reservation.

AUTHOR CONTRIBUTIONS

Methodology and funding acquisition, WC, WW, and WP; software, SX; data curation and formal analysis, XW; visualization, YZ; supervision, QW. All authors have read and agreed to the published version of the manuscript.

FUNDING

This research was funded by the National Natural Science Foundation of China (51974118, 51774132) and the Natural Science Foundation of Hunan Province (2021JJ30265).

ACKNOWLEDGMENTS

We thank Jie Liu, Min Wang and Xiaofan Wu for useful discussions and for early contributions to the project as well as the reviewers for very helpful and inspiring comments.

REFERENCES

Atkinson, B. K., and Meredith, P. G. (1981). Stress Corrosion Cracking of Quartz: A Note on the Influence of Chemical Environment. *Tectonophysics* 77 (1-2), T1–T11. doi:10.1016/0040-1951(81)90157-8

Brzesowsky, R. H., Hangx, S. J. T., Brantut, N., and Spiers, C. J. (2014). Compaction Creep of Sands Due to Time-dependent Grain Failure: Effects of Chemical Environment, Applied Stress, and Grain Size. *J. Geophys. Res. Solid Earth* 119 (10), 7521–7541. doi:10.1002/2014JB011277

Cao, R.-h., Cao, P., Lin, H., Fan, X., Zhang, C., and Liu, T. (2019). Crack Initiation, Propagation, and Failure Characteristics of Jointed Rock or Rock-like Specimens: A Review. *Adv. Civil Eng.* 2019 (6), 1–31. doi:10.1155/2019/6975751

Cao, R.-h., Wang, C., Yao, R., Hu, T., Lei, D., Lin, H., et al. (2020a). Effects of Cyclic Freeze-Thaw Treatments on the Fracture Characteristics of sandstone under Different Fracture Modes: Laboratory Testing. *Theor. Appl. Fracture Mech.* 109, 102738. doi:10.1016/j.tafmec.2020.102738

Cao, R.-h., Yao, R., Hu, T., Wang, C., Li, K., and Meng, J. (2021). Failure and Mechanical Behavior of Transversely Isotropic Rock under Compression-Shear Tests: Laboratory Testing and Numerical Simulation. *Eng. Fracture Mech.* 241, 107389. doi:10.1016/j.engfracmech.2020.107389

Cao, R.-h., Yao, R., Meng, J., Lin, Q., Lin, H., and Li, S. (2020b). Failure Mechanism of Non-persistent Jointed Rock-like Specimens under Uniaxial Loading: Laboratory Testing. *Int. J. Rock Mech. Mining Sci.* 132, 104341. doi:10.1016/j.ijrmms.2020.104341

Cao, S., Zheng, D., Yilmaz, E., Yin, Z., Xue, G., and Yang, F. (2020). Strength Development and Microstructure Characteristics of Artificial concrete Pillar Considering Fiber Type and Content Effects. *Construction Building Mater.* 256**,** 119408. doi:10.1016/j.conbuildmat.2020.119408

Chao, H. M. (2014). Progress and Challenges of Soft Rock Engineering in Depth. *J. China Coal Soc.* 39 (8), 1409–1417. doi:10.13225/j.cnki.jccs.2014.9044

Chen, H., Fan, X., Lai, H., Xie, Y., and He, Z. (2019). Experimental and Numerical Study of Granite Blocks Containing Two Side Flaws and a Tunnel-Shaped Opening. *Theor. Appl. Fracture Mech.* 104, 102394. doi:10.1016/j.tafmec.2019.102394

Chun, W. Y., Yan, W. Y., Guang, L. J., Qi, S. C., and Xiao, S. (2019). Shale Creep Equation Based on Chemical pH Value Characterization. *J. China Coal Soc.* 44(S2), 509–516. doi:10.13225/j.cnki.jccs.2019.0468

Dunning, J., Douglas, B., Miller, M., and McDonald, S. (1994). The Role of the Chemical Environment in Frictional Deformation: Stress Corrosion Cracking and Comminution. *Pageoph* 143 (1), 151–178. doi:10.1007/BF00874327

Einstein, H. H., Hirschfeld, R. C., Nelson, R. A., and Bruhn, R. W. (1969). "Model Studies Of Jointed-Rock Behavior," in The 11th U.S. Symposium on Rock Mechanics (USRMS) (Berkeley, California: American Rock Mechanics Association).

Esterhuizen, G. S., Dolinar, D. R., and Ellenberger, J. L. (2011). Pillar Strength in Underground Stone Mines in the United States. *Int. J. Rock Mech. Mining Sci.* 48 (1), 42–50. doi:10.1016/j.ijrmms.2010.06.003

Fan, X., Jiang, X., Liu, Y., Lin, H., Li, K., and He, Z. (2021a). Local Stress Distribution and Evolution Surrounding Flaw and Opening within Rock Block under Uniaxial Compression. *Theor. Appl. Fracture Mech.* 112, 102914. doi:10.1016/j.tafmec.2021.102914

Fan, X., Yang, Z., and Li, K. (2021b). Effects of the Lining Structure on Mechanical and Fracturing Behaviors of Four-Arc Shaped Tunnels in a Jointed Rock Mass under Uniaxial Compression. *Theor. Appl. Fracture Mech.* 112**,** 102887. doi:10.1016/j.tafmec.2020.102887

Feng, D. H., Yu, Q., lin, L. J., Qiao, J., Assefa, E., and zhe, L. X. (2021). Degradation Mechanism of Intermittent Jointed sandstone under Water-Rock Interaction. *Chin. J. Geotechnical Eng.* 43 (4), 634–643. doi:10.11779/CJGE202104005

Gercek, H. (2007). Poisson's Ratio Values for Rocks. *Int. J. Rock Mech. Mining Sci.* 44 (1), 1–13. doi:10.1016/j.ijrmms.2006.04.011

Hao, R.-q., Li, J.-t., Cao, P., Liu, B., and Liao, J. (2015). Test of Subcritical Crack Growth and Fracture Toughness under Water-Rock Interaction in Three Types of Rocks. *J. Cent. South. Univ.* 22 (2), 662–668. doi:10.1007/s11771-015-2568-9

Jiang, L., and Wen, Y. (2011). Damage Constitutive Model of Sandstone during Corrosion by AMD. *J. Central South Univ. (Sci. Technol.)* 42 (11), 3502–3596. doi:10.1016/S1005-0302(11)60029-7

Lin, Z. Y., yang, Z. L., Jian, L., Weijun, W., Qiang, L., and Liming, T. (2020). Experimental Study of Fracture Toughness and Subcritical Crack Growth of Three Rocks under Different Environments. *Int. J. Geomechanics* 20(8)**,** 04020128. doi:10.1061/(ASCE)GM.1943-5622.0001779

Li, Y., Li, K., Feng, X., and Cai, M. (2018). Development and Evaluation of Artificial Expandable Pillars for Hard Rock Mining. *Int. J. Rock Mech. Mining Sci.* 110, 68–75. doi:10.1016/j.ijrmms.2018.07.014

Liu, H., Zhu, W., Yu, Y., Xu, T., Li, R., and Liu, X. (2020). Effect of Water Imbibition on Uniaxial Compression Strength of sandstone. *Int. J. Rock Mech. Mining Sci.* 127, 104200. doi:10.1016/j.ijrmms.2019.104200

Liu, J., Cao, P., and Han, D. (2016). The Influence of Confining Stress on Optimum Spacing of TBM Cutters for Cutting Granite. *Int. J. Rock Mech. Mining Sci.* 88, 165–174. doi:10.1016/j.ijrmms.2016.07.017

Liu, J., and Jiang, G. (2021). Use of Laboratory Indentation Tests to Study the Surface Crack Propagation Caused by Various Indenters. *Eng. Fracture Mech.* 241, 107421. doi:10.1016/j.engfracmech.2020.107421

Liu, J., Wang, J., and Wan, W. (2018). Numerical Study of Crack Propagation in an Indented Rock Specimen. *Comput. Geotechnics* 96, 1–11. doi:10.1016/j.compgeo.2017.10.014

Miao, S., Cai, M., Guo, Q., Wang, P., and Liang, M. (2016). Damage Effects and Mechanisms in Granite Treated with Acidic Chemical Solutions. *Int. J. Rock Mech. Mining Sci.* 88, 77–86. doi:10.1016/j.ijrmms.2016.07.002

Okubo, S., Fukui, K., and Hashiba, K. (2010). Long-term Creep of Water-Saturated Tuff under Uniaxial Compression. *Int. J. Rock Mech. Mining Sci.* 47(5)**,** 839–844. doi:10.1016/j.ijrmms.2010.03.012

Qiao, L., Wang, Z., and Huang, A. (2017). Alteration of Mesoscopic Properties and Mechanical Behavior of Sandstone Due to Hydro-Physical and Hydro-Chemical Effects. *Rock Mech. Rock Eng.* 50 (2), 255–267. doi:10.1007/s00603-016-1111-0

Wang, F., Cao, P., Cao, R.-h., Xiong, X.-g., and Hao, J. (2019). The Influence of Temperature and Time on Water-Rock Interactions Based on the Morphology of Rock Joint Surfaces. *Bull. Eng. Geol. Environ.* 78 (5), 3385–3394. doi:10.1007/s10064-018-1315-5

Wang, F., Cao, P., Wang, Y., Hao, R., Meng, J., and Shang, J. (2020). Combined Effects of Cyclic Load and Temperature Fluctuation on the Mechanical Behavior of Porous Sandstones. *Eng. Geology.* 266, 105466. doi:10.1016/j.enggeo.2019.105466

Wang, M., and Wan, W. (2019). A New Empirical Formula for Evaluating Uniaxial Compressive Strength Using the Schmidt Hammer Test. *Int. J. Rock Mech. Mining Sci.* 123, 104094. doi:10.1016/j.ijrmms.2019.104094

Wang, Y., Han, J., Ren, J., and Li, C. (2021). Anisotropic Fracture and Energy Dissipation Characteristics of Interbedded marble Subjected to Multilevel Uniaxial Compressive Cyclic Loading. *Fatigue Fract Eng. Mater. Struct.* 44 (2), 366–382. doi:10.1111/ffe.13365

Wu, Q., Chen, L., Shen, B., Dlamini, B., and Zhu, Y. (2019a). Experimental Investigation on Rockbolt Performance Under the Tension Load. *Rock Mech. Rock Eng.* 52 (11), 4605–4618. doi:10.1007/s00603-019-01845-1

Wu, Q., Weng, L., Zhao, Y., Guo, B., and Luo, T. (2019b). On the Tensile Mechanical Characteristics of fine-grained Granite after Heating/cooling Treatments with Different Cooling Rates. *Eng. Geology.* 253, 94–110. doi:10.1016/j.enggeo.2019.03.014

Wu, Q., Weng, L., Zhao, Y., Zhao, F., Peng, W., and Zhang, S. (2020). Deformation and Cracking Characteristics of Ring-Shaped Granite with Inclusion under Diametrical Compression. *Arab J. Geosci.* 13 (14), 681. doi:10.1007/s12517-020-05718-8

Xie, S., and Wan, W. (2020). Mechanical Damage to the Diorite Caused by Acid Corrosion. *Geotech Geol. Eng.* 38 (3), 3087–3094. doi:10.1007/s10706-020-01209-5

Yang, S. Q., and Liu, X. R. (2012). Experimental Investigation on Dilatancy Behavior of marble with Pre-existing Fissures under Different Confining Pressures. *Chin. J. Geotechnical Eng.* 34 (12), 2188–2197.

Zhang, J.-Z., and Zhou, X.-P. (2020a). AE Event Rate Characteristics of Flawed Granite: from Damage Stress to Ultimate Failure. *Geophys. J. Int.* 222, 795–814. doi:10.1093/gji/ggaa207

Zhang, J.-Z., and Zhou, X. P. (2020b). Forecasting Catastrophic Rupture in Brittle Rocks Using Precursory AE Time Series. *J. Geophys. Res. Solid Earth* 125 (8), e2019JB019276. doi:10.1029/2019JB019276

Zhang, J.-Z., Zhou, X. P., Zhou, L. S., and Berto, F. (2019). Progressive Failure of Brittle Rocks with Non-isometric Flaws: Insights from Acousto-optic-mechanical (AOM) Data. *Fatigue Fract Eng. Mater. Struct.* 42 (8), 1787–1802. doi:10.1111/ffe.13019

Zhang, J., Peng, J., Zheng, J., Dai, L., and Yao, Y. (2019). Prediction of Resilient Modulus of Compacted Cohesive Soils in South China. *Int. J. Geomech.* 19 (7), 04019068. doi:10.1061/(ASCE)GM.1943-5622.0001446

Zhang, J., Zhang, A., Huang, C., Yu, H., and Zhou, C. (2021). Characterising the Resilient Behaviour of Pavement Subgrade with Construction and Demolition Waste under Freeze-Thaw Cycles. *J. Clean. Prod.* 300, 126702. doi:10.1016/j.jclepro.2021.126702

Zhang, Z., Huang, X., Liu, W., Wang, L., and Xiao, M. (2020). Study on the Hydraulic Parameters of Woshaxi Landslide Soils during Water Level Drawdown of Three Gorges Reservoir. *Geofluids* 2020 (1), 1–14. doi:10.1155/2020/6283791

Zhao, Y., Liu, Q., Zhang, C., Liao, J., Lin, H., and Wang, Y. (2021a). Coupled Seepage-Damage Effect in Fractured Rock Masses: Model Development and a Case Study. *Int. J. Rock Mech. Mining Sci.* 144, 104822. doi:10.1016/j.ijrmms.2021.104822

Zhao, Y., Wang, Y., Wang, W., Tang, L., Liu, Q., and Cheng, G. (2019a). Modeling of Rheological Fracture Behavior of Rock Cracks Subjected to Hydraulic Pressure and Far Field Stresses. *Theor. Appl. Fracture Mech.* 101 (12), 59–66. doi:10.1016/j.tafmec.2019.01.026

Zhao, Y., Wang, Y., Wang, W., Tang, L., Liu, Q., and Cheng, G. (2019b). Modeling of Rheological Fracture Behavior of Rock Cracks Subjected to Hydraulic Pressure and Far Field Stresses. *Theor. Appl. Fracture Mech.* 101, 59–66. doi:10.1016/j.tafmec.2019.01.026

Zhao, Y., Zhang, C., Wang, Y., and Lin, H. (2021b). Shear-related Roughness Classification and Strength Model of Natural Rock Joint Based on Fuzzy Comprehensive Evaluation. *Int. J. Rock Mech. Mining Sci.* 137, 104550. doi:10.1016/j.ijrmms.2020.104550

Zhao, Y., Zhang, L., Wang, W., Pu, C., Wan, W., and Tang, J. (2016). Cracking and Stress-Strain Behavior of Rock-like Material Containing Two Flaws Under Uniaxial Compression. *Rock Mech. Rock Eng.* 49 (7), 2665–2687. doi:10.1007/s00603-016-0932-1

Zhao, Y., Zhang, L., Wang, W., Tang, J., Lin, H., and Wan, W. (2017). Transient Pulse Test and Morphological Analysis of Single Rock Fractures. *Int. J. Rock Mech. Mining Sci.* 91, 139–154. doi:10.1016/j.ijrmms.2016.11.016

Zhao, Z., Guo, T., Ning, Z., Dou, Z., Dai, F., and Yang, Q. (2018). Numerical Modeling of Stability of Fractured Reservoir Bank Slopes Subjected to Water-Rock Interactions. *Rock Mech. Rock Eng.* 51 (8), 2517–2531. doi:10.1007/s00603-017-1360-6

Zhou, X.-P., Li, L. H., and Berto, F. (2019b). Cracking Behaviors of Rock-like Specimens Containing Two Sets of Preexisting Cross Flaws under Uniaxial Compression. *J. Test. Eval.* 47 (2), 838–867. doi:10.1520/jte20170358

Zhou, X.-P., and Zhang, J.-Z. (2021). Damage Progression and Acoustic Emission in Brittle Failure of Granite and sandstone. *Int. J. Rock Mech. Mining Sci.* 143, 104789. doi:10.1016/j.ijrmms.2021.104789

Zhou, X.-P., Zhang, J.-Z., Qian, Q.-H., and Niu, Y. (2019a). Experimental Investigation of Progressive Cracking Processes in Granite under Uniaxial Loading Using Digital Imaging and AE Techniques. *J. Struct. Geology.* 126, 129–145. doi:10.1016/j.jsg.2019.06.003

Zhou, X.-P., Zhang, J.-Z., and Wong, L. N. Y. (2018). Experimental Study on the Growth, Coalescence and Wrapping Behaviors of 3D Cross-Embedded Flaws Under Uniaxial Compression. *Rock Mech. Rock Eng.* 51 (5), 1379–1400. doi:10.1007/s00603-018-1406-4

Conflict of Interest: The authors declare that the research was conducted in the absence of any commercial or financial relationships that could be construed as a potential conflict of interest.

Publisher's Note: All claims expressed in this article are solely those of the authors and do not necessarily represent those of their affiliated organizations, or those of the publisher, the editors and the reviewers. Any product that may be evaluated in this article, or claim that may be made by its manufacturer, is not guaranteed or endorsed by the publisher.